Physics in Medicine & Biology

Anatomical deformation due to horizontal rotation: towards gantry-free radiation therapy

Anatomical deformation due to horizontal rotation: Towards gantry-free radiation therapy

J. G. Buckley[1,3], R. Rai[3,4], G. P. Liney[1,2,3,4], J. A. Dowling[1,2,5], L. C. Holloway[1,2,3,4], P. E. Metcalfe[1,3], P. J. Keall[3,6]

[1] Centre For Medical Radiation Physics, University of Wollongong, NSW, Australia

[2] University of New South Wales, School of Medicine, Sydney, Australia

[3] Ingham Institute for Applied Medical Research, Liverpool, Australia

[4] Liverpool Hospital Cancer Therapy Centre, South West Sydney Local Health District, Liverpool, Australia

[5] CSIRO Australian eHealth Research Centre, Herston, Australia

[6] ACRF Image-X Institute, School of Medicine, University of Sydney, Sydney, Australia

Key Words: Patient Rotation, MRI-guided Radiotherapy, MRI-Linac, Anatomical Deformation, Image-Guided Radiotherapy

Running Title: *Anatomical deformation due to horizontal rotation for MRIgRT*

Word count no references: 5269

Word count: 6188

Number of figures: 14

Number of tables: 3

Abstract

Gantry-free radiation therapy systems may be simpler and more cost effective, particularly for MRI-guided photon or hadron therapy. This study aims to understand and quantify anatomical deformations caused by horizontal rotation with scan sequences sufficiently short to facilitate integration into an MRI-guided workflow.

Rigid and non-rigid pelvic deformations due to horizontal rotation were quantified for a cohort of 8 healthy volunteers using a bespoke patient rotation system and a clinical MRI scanner. For each volunteer a reference scan was acquired at 0° followed by sequential faster scans in 45° increments through to 360°. All fast scans were registered to the 0° image via a 3-step process: First, images were aligned using MR visible couch markers. Second, the scans were pre-processed then rigidly registered to the 0° image. Third, the rigidly registered scans were non-rigidly registered to the 0° image to assess soft tissue deformation. The residual differences after rigid and non-rigid registration were determined from the transformation matrix and the deformation vector field, respectively.

The rigid registration yielded mean rotations of ≤ 2.5° in all cases. The average 3D translational magnitudes range was 5.8 ± 2.9 mm - 30.0 ± 11.0 mm. Translations were most significant in the left-right direction. Smaller translations were observed in the anterior-posterior and superior-inferior directions. The maximum deformation magnitudes range was: 10.0 ± 0.9 mm - 28.0 ± 2.8 mm and average deformation magnitudes range: 2.3 ± 0.6 mm - 7.5 ± 1.0 mm. Average non-rigid deformation magnitude was correlated with BMI (correlation coefficient 0.84, $p = 0.01$).

Rigid pelvic deformations were most significant in the left-right direction but could be accounted for with on-line adjustments. Non-rigid deformations can be significant and will need to be accounted for in order to facilitate the delivery of gantry-free therapy with an automated patient rotation system.

Introduction

Conventional external beam radiation therapy (EBRT) utilises a modulated x-ray beam rotated about the patient to deliver a highly conformal treatment. An alternative approach involving a fixed radiation beam (gantry-free) would greatly simplify the engineering and cost barriers[1] associated with rotating gantries[2] both in terms of simplified linac design, particularly for hadron therapy[3], and reduced complexity of coupling between the linac and the magnetic field of emerging MRI-Linac systems[4-6]. Radiation shielding requirements would also be reduced with gantry-free systems since the primary beam is only incident on a single wall. A prototype system using a horizontal patient rotation system coupled to a clinical linac has already been developed and the proof of concept demonstrated[7-10].

It's not clear how well cancer patients would tolerate rotation, particularly patients who are very unwell or elderly. A recent study by Whelan *et al.* demonstrated rotation may be well tolerated by cancer patients[11], however the addition of MRI may add further feelings of anxiety[12] and claustrophobia[13]. Treatments using a gantry-free x-ray source and patient rotation would also require fundamental changes in how treatment plans are created. The current workflow is typically to acquire a planning computed tomography (CT) scan with the patient set up in the treatment position, then to create a treatment plan on this scan using multiple beam angles and modulation of beam weightings via an optimisation algorithm[14]. In a gantry-free system, images would be acquired at each couch angle and a modulated field would be optimised for each angle. The dose optimisation and calculation would then need to be applied to a summation of each couch position akin to dose calculation with 4D CT and respiratory binning[15].

A further challenge, particularly with horizontal patient rotation, is the introduction of soft tissue deformation due to gravity[16,17] which has been demonstrated to affect organ positioning and dosimetry in prone vs supine position[18]. It has been suggested that the impact would be most significant on the external body contour, particularly for the pelvis during EBRT for prostate and cervical treatment[16]. The change in external contour will shift the penetration depth of the x-ray beam and compromise treatment if not accounted for[19]. Lagomorph studies using horizontal rotation and kilo-voltage Cone Beam CT (kV CBCT) imaging system have assessed thoracic motion due to rotation[20,21] and found the most significant motion was rigid shifts in the anterior-posterior direction, however it would be expected that external soft tissue deformation would be more significant for humans. Whelan et al assessed changes in the prostate, rectum and bladder contours of a single volunteer[17] and found up to 4 mm variation in the mean average surface distance which could be largely mitigated by a prostate-guided rigid shift. The global rigid and non—rigid soft tissue deformation of human anatomy due to horizontal rotation have not yet been quantified and must be understood if horizontal rotation is to be used for treatment for reasons described above.

The aim of this study is to quantify rigid and non-rigid deformation of the pelvis due to horizontal rotation in a cohort of healthy volunteers using a bespoke patient rotation system on a commercial MRI scanner.

Methods

An ethics-approved study (ACTRN12618000676213) was undertaken with 8 healthy volunteers whose volunteer demographic information is summarised in Table 1. As there is little published data on the magnitude of anatomic deformation during rotation the sample size was pragmatically chosen to obtain sufficient information but not expose human subjects to unnecessary scans. Eligibility criteria included no contraindication to MRI, weight not exceeding 100 Kg, height not exceeding 190 cm, a total anterior-posterior width not exceeding 32 cm and a total lateral width not exceeding 46 cm where the PRS canopy covers the volunteer.

Table 1: Healthy volunteer demographics

Volunteer ID	Age	Gender	Height (cm)	Weight (Kg)	Body mass index
1	26	F	154	52	21.9
2	26	F	160	56	21.8
3	26	F	158	57	22.8
4	27	F	155	41	17.1
5	40	F	162	59	22.4
6	30	M	175	70	22.9
7	35	F	178	75	23.7
8	46	F	167	76	27.3

Volunteers were imaged on a 64-channel, closed, wide-bore 3 Tesla (MAGNETOM Skyra, Siemens, Erlangen, Germany) dedicated radiation therapy MRI scanner (Siemens Medical Systems, Erlangen, Germany) in a previously described bespoke patient rotation system (PRS)[17].

Volunteers were secured within the PRS using polyester straps and three airbags. Once secure, the volunteers were rotated outside of the MRI scanner to ensure clearance during the rotation and to familiarise the volunteer with the rotation prior to imaging. The volunteers were then moved into the MRI scanner and underwent the imaging procedure summarised in Figure 1 .

Figure 1: Workflow of the PAROT study. The volunteer was first loaded into the patient rotation system and secured. An isotropic scan was then acquired in the supine (0° rotation) position before being manually adjusted in 45° increments. A faster scan was acquired in the supine (0° rotation) position before being manually adjusted in 45° increments. A faster scan was acquired at each position.

All sequences acquired in this study used the integrated body coil to both transmit and receive radiofrequency (RF) signal. Initially, a single high-quality isotropic T2-weighed turbo spin echo (TSE) isotropic SPACE (Sampling Perfection with Application optimised Contrasts using different flip angle Evolution) scan with a voxel size of 1.7×1.7×1.7 mm^3, TE/TR of 103/1470 ms, 500 mm^2 field of view (FOV), 780 Hz/Px receiver bandwidth and an approximate scan time of 6 minutes. This scan was acquired in the supine position (defined here as 0° rotation) and used as the target image to which subsequent images were registered.

The PRS was then manually rolled to the volunteers right in 45° increments from 45° - 360° with the volunteer re-scanned at each position using a faster T2-weighted TSE scan with a voxel size of 2.0×2.0×4 mm^3, TE/TR of 96/12170 ms, 500x500 mm^2 FOV, 405 Hz/px receiver bandwidth and an approximate scan time of 55 seconds. Fast scans were used for the rotated images to reduce the time a volunteer was positioned in the angled positions. Vendor supplied 3D geometric distortion corrections and an anatomical site specific B1 shim (Trueform) were applied to all images. The scans were then exported from the MRI scanner and an external contour generated on each image using tools from MiM picture archiving and communication system (version 6.8, MIM Software Inc., Cleveland, OH, USA).

The images and their respective external contours were then exported from MiM and manually re-orientated to the 0° coordinate space using MR visible markers placed on the PRS in 3DSlicer[22]. The images were then resampled to the isotropic 0° scan for registration. Image information outside of the external contours, i.e. noise and motion artefact, were removed by masking each image with the respective body contour. Images then underwent a bias field correction[23] to remove variations in signal intensity and a histogram normalisation to the 0° image to aid registration. Pre-processing was performed using tools from the Insight Toolkit (https://itk.org).

Rigid Motion Assessment

Rigid motion was quantified through the registration of each volunteer's couch marker aligned image to their respective 0° image using *mirorr*[24], an open source rigid/affine registration algorithm developed for MR-CT registration. The algorithm has the benefit of inverse consistency using a block matching registration approach and mid-space image resampling. The resulting transform were analysed in MATLAB (MathWorks Inc., Natick, MA) to assess pitch, yaw and roll rotations and translation in left-right (LR), anterior-posterior (AP) and superior-inferior (SI) axis as shown in Figure 2.

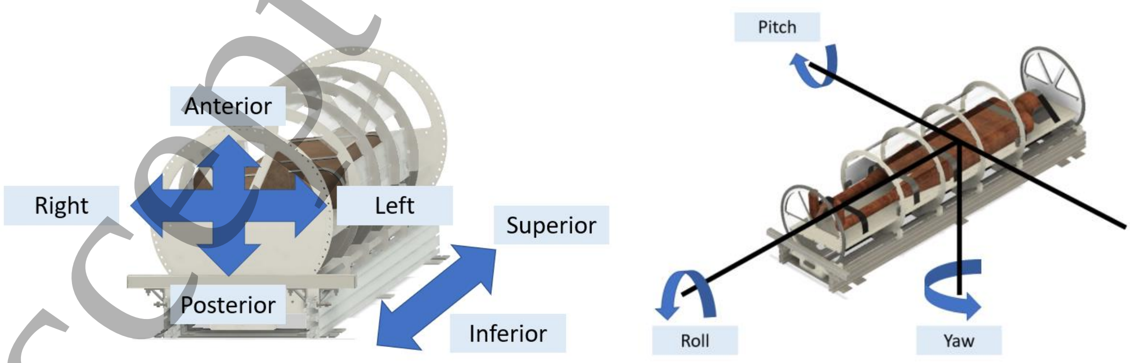

Figure 2: Rigid translation and rotations within the patient rotation system. Right and left orientations are relative to the volunteer physical supine orientation.

The rigid registration workflow was validated using a CIRS Model 048 male pelvis multi-modality phantom (Imaging Solutions©). The phantom includes pelvic bones, 177cc anechoic bladder, prostate, urethra, seminal vesicles and rectum. Manual offsets of ± 5 mm, 10 mm, 30 mm and 50 mm were introduced in the LR and SI planes and compared to translations from the transformation matrix following registration to the centred phantom image. LR offsets were achieved by alignment with in-room lasers with corresponding shifts applied and SI offsets by adjustment of the patient table on the console. AP motion was not assessed as the MRI couch could not be incrementally adjusted, and it was concluded that any discrepancy between the measured and registration translations would be apparent using the LR and SI directions.

Non-Rigid Deformation Assessment

Residual soft tissue deformation was assessed by non-rigidly registering each rigidly registered image to the corresponding 0° image using deformable registration. The algorithm used is based on a cubic B-spline free-deformation model using a normalised mutual information metric from the non-commercial open source software NiftyReg (NiftyReg version 1.3.9)[25]. A displacement vector field was generated from the registration and analysed in MATLAB. Due to SI variations in the anatomy captured by the FOV between the 0° and angled scans, a SI mask was created on each of the 2D scans following pre-processing using the itk interface package ITK-SNAP[26] (http://www.itksnap.org). Each SI mask was then resampled to the rigidly registered image using the transform from the rigid registration. The rigidly resampled SI mask was then applied to the rigidly registered image and the 0° image to create a pair of anatomically equivalent images for the non-rigid registration. The entire process is summarised in Figure 3.

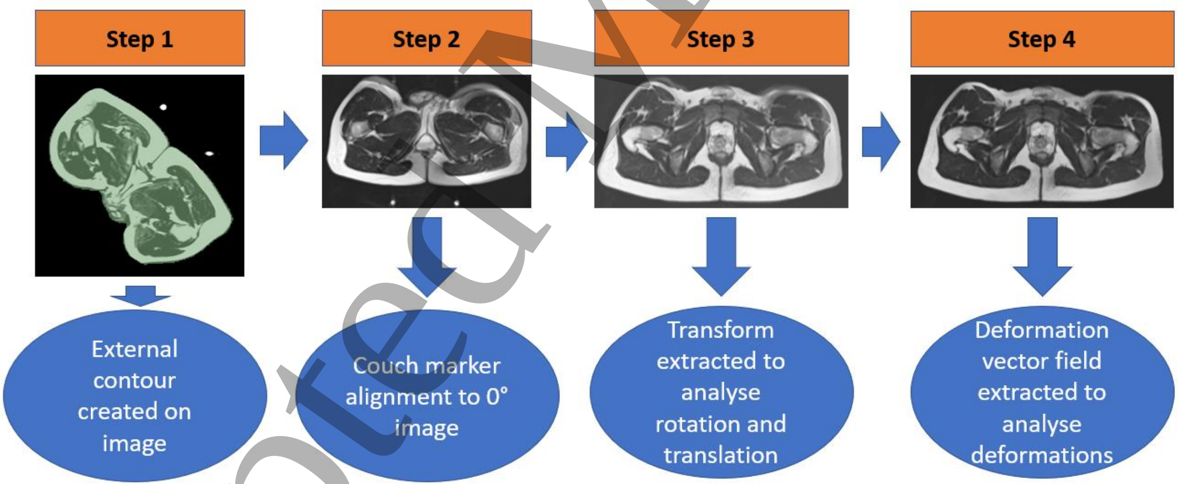

Figure 3: Image registration workflow. Step 1: An external contour was generated for each image using the MiM external body contour tool. Step 2: couch marker alignment to the respective 0° scan. Step 3: Images were masked with their respective external contour to remove image artefacts outside the body before pre-processing then rigidly registered to the 0° image. Step 4: SI masking was applied to the rigidly registered image and the 0° scan before non-rigid registration of the rigidly registered image to the 0° image. Transform files and deformation vector fields were exported to analyse the rigid and non-rigid motion respectively.

The accuracy of the non-rigid registration was evaluated on the two volunteers with the highest and lowest BMI scores (volunteer 8 and volunteer 4) by comparing external body contours, where maximum non-rigid deformation was expected to occur, and bladder contours as shown in Figure 4. The contours were generated on the original rotated images using the contouring toolkit in MiM then propagated to the non-rigidly registered images using transform files and DVF's from the rigid and non-rigid image registrations, respectively. Finally, the propagated contours were compared to those generated on the 0° reference image with dice similarity coefficient (DSC) and the maximum average Hausdorff distance between contour surfaces, as suggested by the AAPM TG132 report[27]. Metrics were calculated using Plastimatch[28].

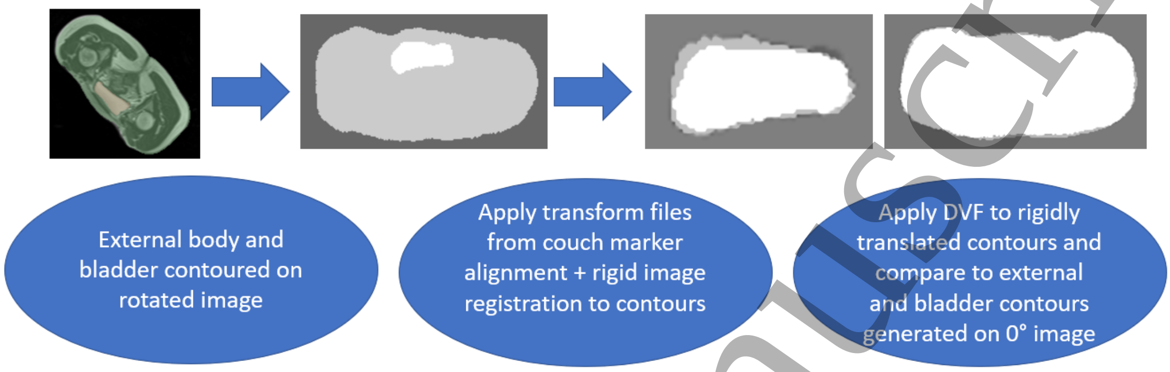

Figure 4: External contour and bladder generation and propagation workflow.

The impact of image distortion and RF non-uniformity on the external body contour due to B0 and B1 magnetic field inhomogeneities, respectively, as the volunteer was rotated off axis during imaging was quantified by imaging a 20-litre plastic phantom filled with cooking oil (30×30×15 cm^3) on the PRS. The imaging sequences and registration workflow used for the volunteers was applied to the phantom images, with an added step of applying a binary filter to the images prior to the registration to remove the impact of air bubbles and fluid flow within the phantom impacting the registration. Images were acquired with the phantom rotated to 0, 90, 180 and 270 degrees.

ΔB0 was evaluated using a gradient field mapping sequence acquired with TE's of 10 ms and 12.46 ms echo (ΔTE = 2.46 ms), TR 1000 ms, 2.5 mm in-plane resolution, 200 x 200 matrix. A period of 10 minutes between repositioning the phantom at each angle and imaging was applied to ensure the oil had settled within the phantom. Both magnitude and phase images were obtained with the latter used to provide phase difference maps (in radians) within the phantom and converted to frequency. Images were displayed with a colour threshold of > 100 Hz of frequency difference.

RF uniformity was assessed in the first magnitude image by comparing the mean signal within a cylindrical ROI in the centre of the phantom to pixel intensities within the phantom following the method described by Liney et al.[29]. Images were displayed using a three-colour scale to indicate whether pixels were > ± 5% ± 5%-10% or < ± 10% of the mean ROI signal intensity.

Correlation between average non-rigid deformation across all couch angles and body max index (BMI) was assessed using a Pearson's correlation coefficient. The quality of the linear fit was quantified using R-squared and adjusted R-squared metrics.

Results

Rigid Motion

Average rigid motion is summarised in Table 2. Rigid left-right (LR), anterior-posterior (AP) and superior-inferior (SI) translations from the rigid registration are shown in Figure 5 (a)-(c). The rigid registration yielded mean rotations of ≤ 2.5° in all cases. Translations were most significant in the LR direction (average magnitude range: 4.9 ± 6.1 mm (volunteer 6) - 29.0 ± 32.0 mm (volunteer 3)). Smaller translations were observed in the AP (range: 2.2 ± 1.4 mm (volunteer 6) - 8.6 ± 5.0 mm (volunteer 8)) and SI directions (range: 0.9 ± 1.2 mm (volunteer 6) - 5.7 ± 3.6 mm (volunteer 4)).

Table 2: Rotations, translations and 3D displacement magnitudes averaged over the 8 rotations following rigid registration.

Volunteer ID	Pitch (°)	Yaw (°)	Roll (°)	LR Translations (mm)	AP Translations (mm)	SI Translations (mm)	3D Displacement Magnitudes (mm)
1	0.45	1.2	0.61	13.0	6.7	2.7	17.0
2	1.3	1.4	1.4	12.0	5.2	1.2	13.0
3	1.0	1.8	2.4	29.0	8.2	1.3	30.0
4	1.0	2.5	2.0	22.0	6.5	5.7	25.0
5	0.63	0.70	0.55	15.0	5.0	2.7	17.0
6	0.31	0.42	0.84	4.9	2.2	0.91	5.8
7	0.44	1.2	0.85	20.0	3.6	1.0	21.0
8	0.79	1.1	1.6	19.0	8.6	2.1	21.0

The magnitude of the rigid shifts varied between the volunteers with average 3D displacement range: 5.8 ± 2.9 mm (volunteer 6) - 30.0 ± 11.0 mm (volunteer 3). No correlation was present between 3D displacement magnitude and volunteer BMI.

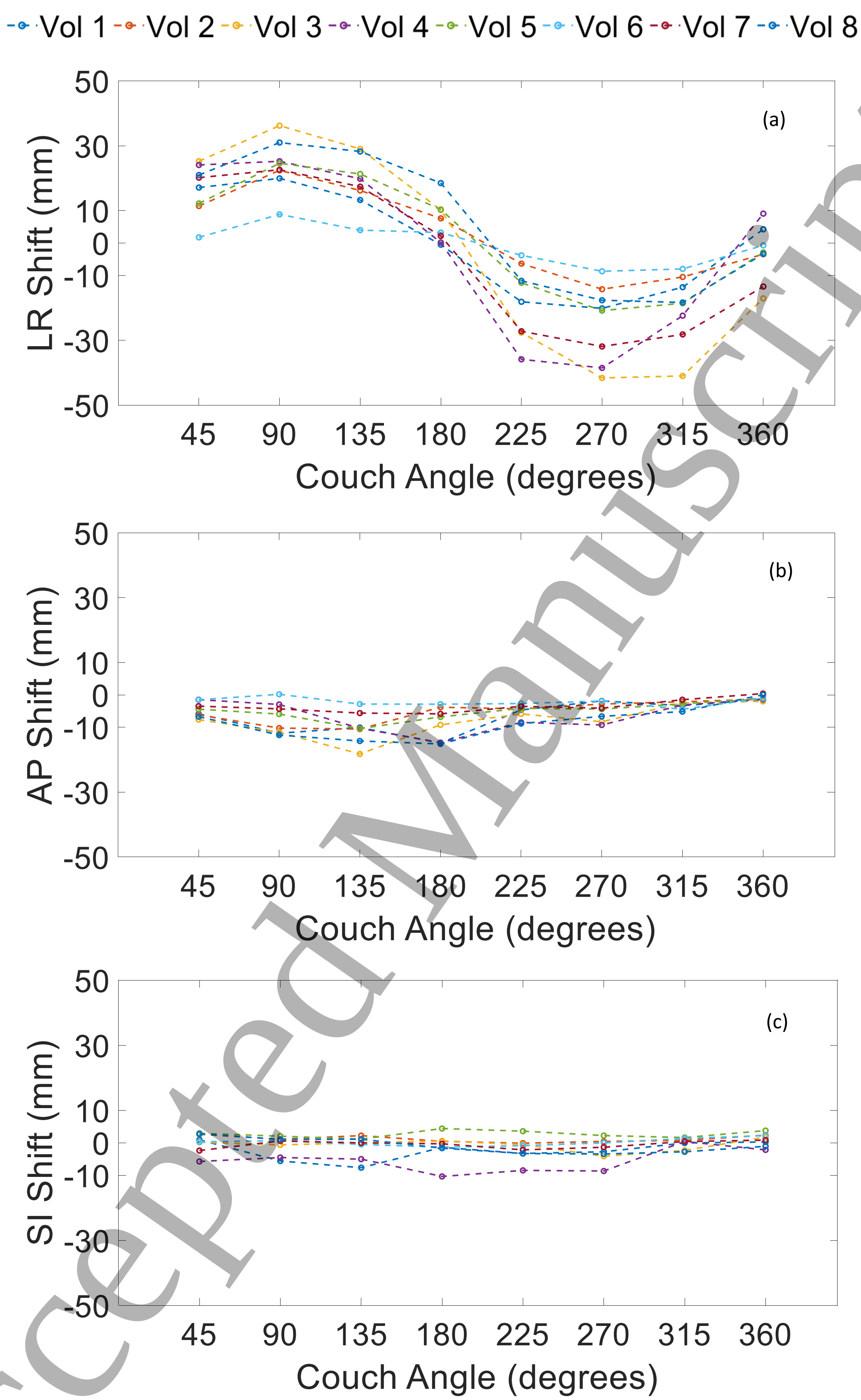

Figure 5: (a) Left-Right (b) Anterior-Posterior and (c) Superior-Inferior translations of each volunteer during rotation. Motion was most significant for the left-right axis and varied sinusoidally with couch angle.

Rigid Registration Validation

A comparison of measured and expected offsets of the CIRS pelvis phantom are shown in Figure 6. Mean differences of -2.0 mm and -2.3 mm between measured and expected values for LR and SI offsets were observed, respectively.

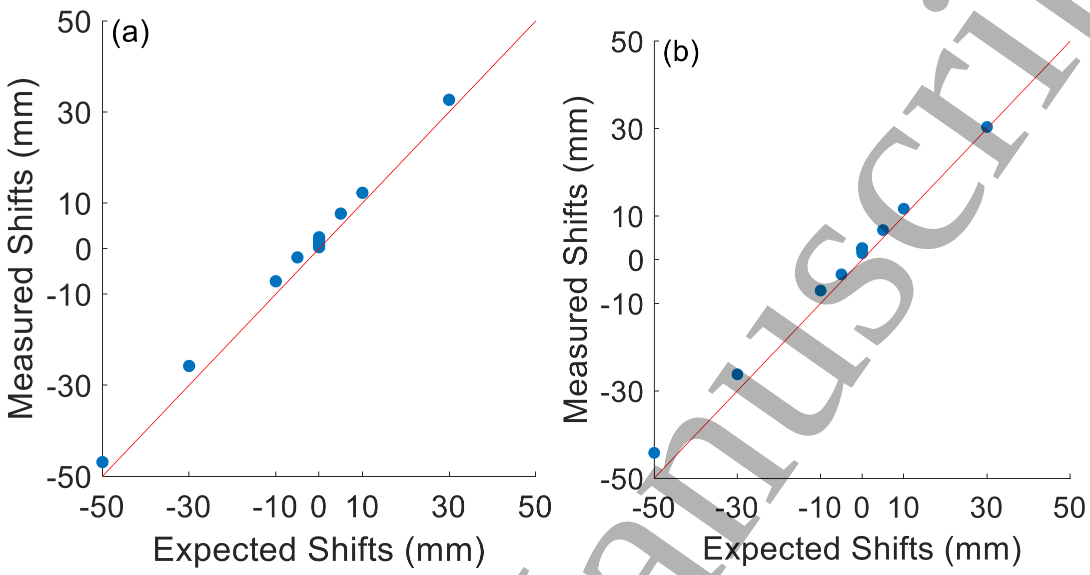

Figure 6: Applied shifts of the CIRS pelvis phantom and values from the rigid registration transform file following registration to the centred phantom position in the (a) left-right and (b) superior-inferior directions. A gradient = 1 line is overlaid indicating 100% agreement. A small systematic offset in the left and superior direction was observed due to shifts in the flat-top on the MRI couch during re-positioning and variation in the laser position relative to the markings on the phantom.

Non-Rigid Deformation

Maximum and average non-rigid deformation magnitudes are summarised in Figure 7 and varied greatly depending on the volunteer (average maximum deformation magnitudes range: 10.0 ± 0.9 mm (volunteer 4) - 28.0 ± 2.8 mm (volunteer 8), average deformation magnitudes range: 2.3 ± 0.6 mm (volunteer 4) - 7.5 ± 1.0 mm (volunteer 8)). Deformation were concentrated on the external surface due to compression or sagging during rotation as seen in the overlay of the volunteer eight 135° image with the 0° image (Figure 8) following each step of the registration. Changes in the external surface following the rigid registration are seen on the anterior and the right sides. Axial, coronal and sagittal views of the highest deformation scan, healthy volunteer 8 90°, with overlaid displacement fields are shown in Figure 9.

Deformation magnitude histograms for the 8 volunteers are shown in Figure 10. The variation in deformation magnitude across the volunteers is again demonstrated, with the 50% deformation magnitude varying between 3 mm for volunteers 1 and 7 mm for volunteer 8 and the 20% deformation magnitudes of 4 mm and 10 mm for the same volunteers as indicated by red and blue lines.

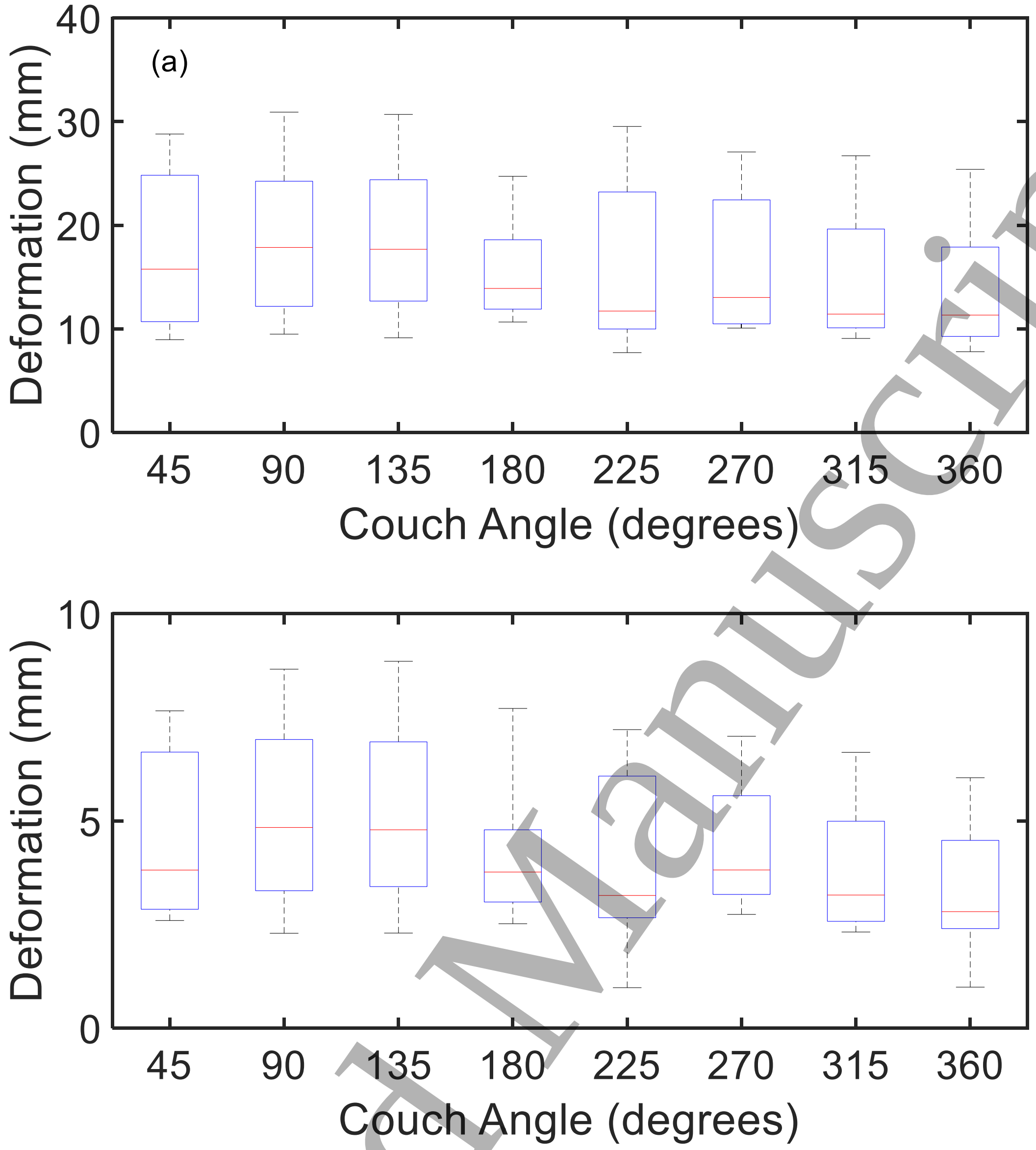

216

Figure 7: Boxplots of (a) maximum and (b) average deformation magnitudes following the non-rigid registration to the 0° isotropic image. Maximum deformation depended greatly on volunteer. Mean deformation were less than 9 mm for all volunteers.

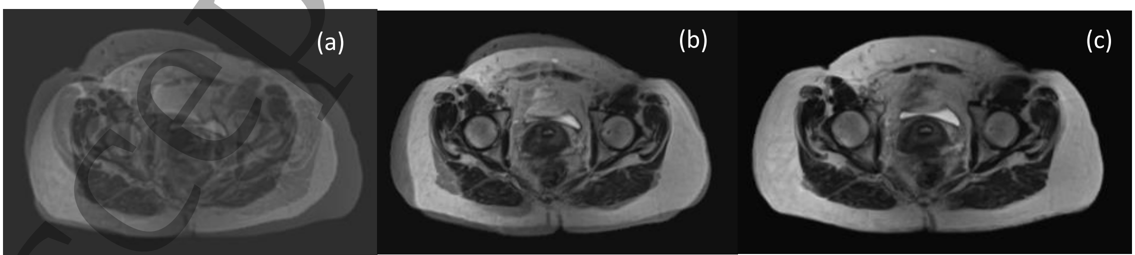

Figure 8: Overlay of volunteer eight 0° image with the 180° image following (a) couch marker alignment (b) rigid registration and (c) non-rigid registration. The rigid registration aligns the rigid anatomy while the variation in the external contour is still clearly visible prior to non-rigid registration.

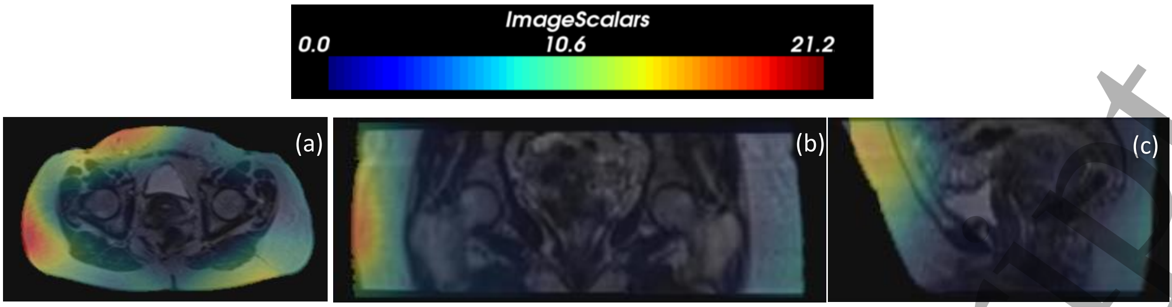

Figure 9: Volunteer eight 90° non-rigidly registered image overlaid with the deformation vector field for (a) axial, (b) coronal and (c) sagittal slices. Non-rigid deformation up to 21 mm were present on the anterior and right external surfaces due to compression under rotation with much smaller deformation internally. Images were generated using the sMilx biomedical image analysis framework[30].

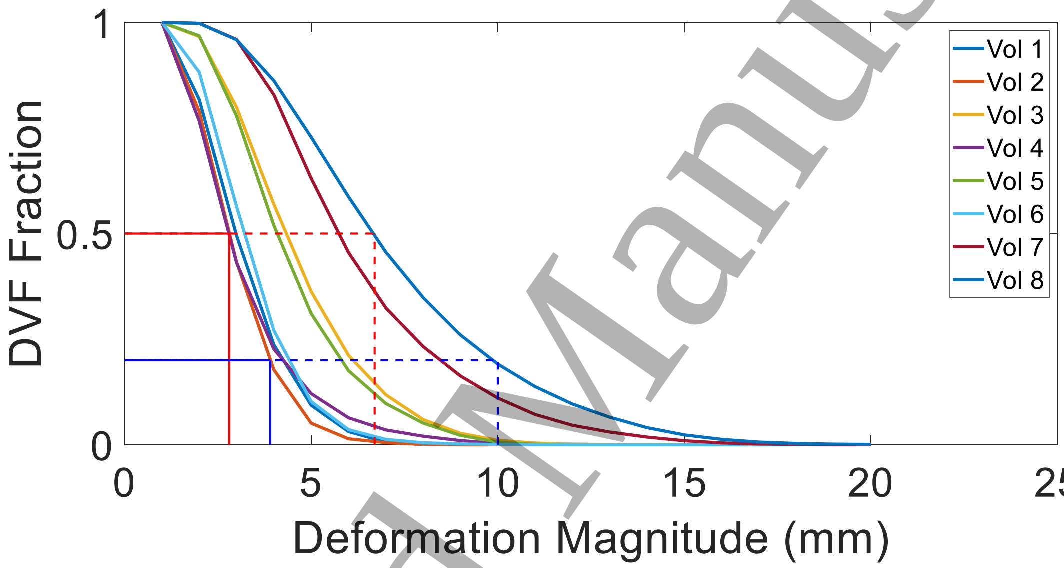

Figure 10: Cumulative histograms of volunteer 3D deformation magnitudes as a fraction of the total deformation vector field. For volunteers 1, 2, 4, and 6 deformation were mostly below 5 mm while for volunteer 8 deformation up to 15 mm are still visible. The 50% and 20% deformation lines for volunteers 1 (solid line) and volunteer 8 (dashed line) with values of 3 mm, 7 mm, 4 mm and 10 mm are overlaid in red and blue, respectively.

Non-Rigid Registration Validation

The mean ± 1 standard deviation DSC and maximum average Hausdorff distance values for the bladder and external contours of the non-rigidly registered images and the respective reference 0-degree images for volunteers 4 and 8 are shown in Table 3:

Table 3: Comparison of average bladder and external body contours for volunteers with the highest and lowest BMI scores (volunteer 8 and volunteer 4), with respect to the 0° reference image contours. Values are quoted with one standard deviation.

Volunteer	Bladder		External Body Contour	
	DSC	Maximum Average Hausdorff Distance (mm)	DSC	Maximum Average Hausdorff Distance (mm)
HV04	0.78 ± 0.04	2.7 ± 0.4	0.98 ± 0.01	1.0 ± 0.2
HV08	0.50 ± 0.07	6.8 ± 1.6	0.99 ± 0.00	0.7 ± 0.1

Image Quality Phantom Measurements

The average external deformation magnitude on the oil filled plastic phantom for all angles was 0.2 ± 0.1 mm and average maximum value 3.8 ± 0.9 mm with the highest results at couch positions 90° (maximum 4.9 mm) and 315° (maximum 4.8 mm). No significant distortion in the shape of the phantom was visually apparent as shown in Figure 11. The regions where the deformation magnitude was greatest corresponded to the points on the phantom which were furthest from the imaging isocentre.

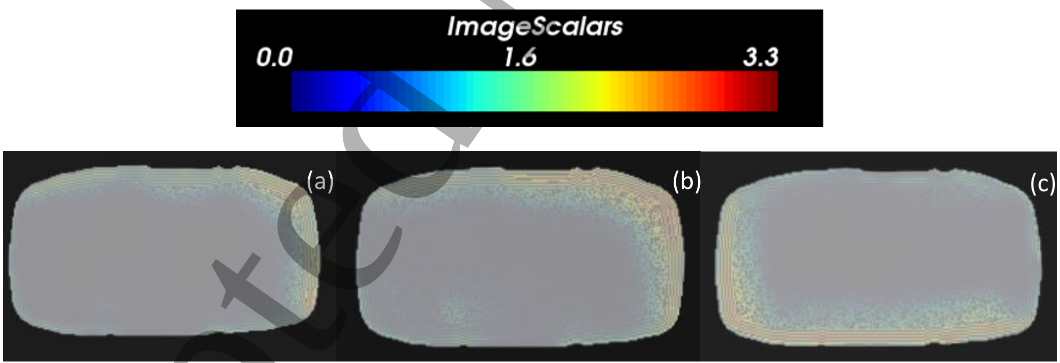

Figure 11: Deformation images of the oil filled phantom at (a) the 90°, (b) 180° and (c) 270° positions following alignment back to the 0-degree position using MR visible markers. No significant distortion of the image was present for any of the scans with maximum deformation below 5 mm in all cases.

Frequency difference maps for angles 0, 90, 180 and 270 degrees are shown in Figure 12:

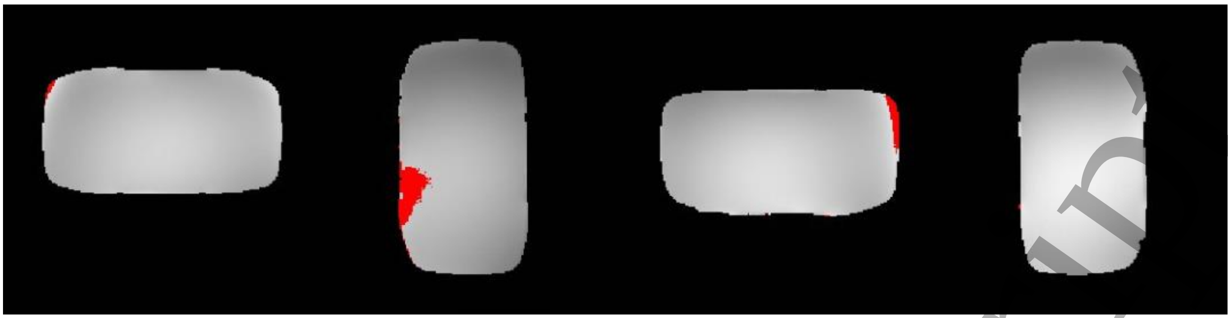

Figure 12: Frequency difference map images of the phantom at 0, 90, 180 and 270 degrees. Red indicates regions with greater than 100 Hz frequency difference. The largest difference on any image (184 Hz) corresponds to a distortion of 0.47 of pixels (for a nominal bandwidth = 395 Hz/pixel).

The majority of frequency differences for each phantom angle were below 100 Hz. The largest phase difference observed on any image was 184 Hz which corresponded to less than half a pixel of distortion.

B1 field uniformity maps for the same angles are shown in Figure 13:

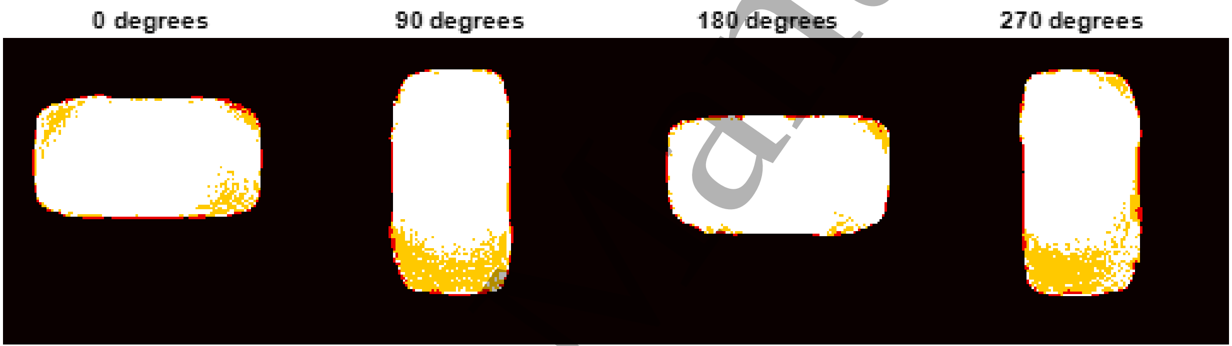

Figure 13: uniformity (B1) maps for phantom images at 0, 90, 180 and 270 degrees. Red, orange and white indicates signal < ± 90%, ± 90%-95% and > ± 95% of the mean ROI signal, respectively.

RF signal was within ± 10% of the mean signal within an ROI in the centre of the phantom for each phantom position with the greater signal loss at the edges of the phantom. The majority of the signal was within ± 5% of the centre ROI.

246 BMI and Non-Rigid Deformation

247 A correlation between volunteer BMI and average non-rigid deformation was observed (Figure 14)
248 (correlation coefficient 0.85 p = 0.01).

249

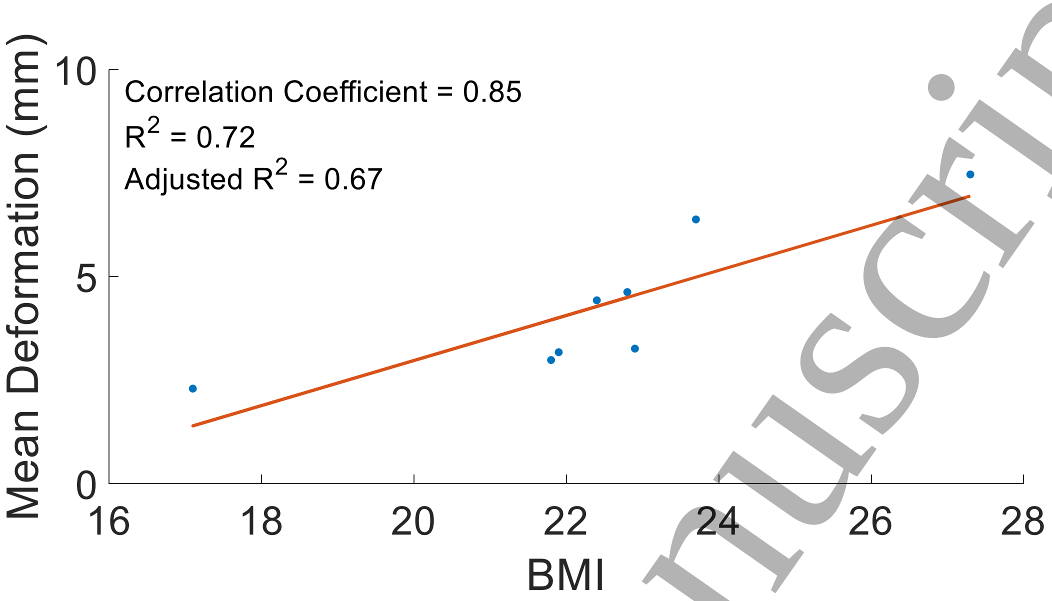

250

Figure 14: Correlation between body mass index (BMI) and mean deformation. A correlation was observed (0.85 p = 0.01), however is limited by the small data set (adjusted R^2 = 0.67) and small variability in BMI values (σ = 2.8).

251

252

Discussion

Rigid motion caused by rotation was predominantly in the left-right direction, likely due to shifts of the entire volunteer within the airbag supports. This finding was supported by Barber *et al.* who observed the same trends on a smaller scale in a lagomorph study[20]. The motion could be reduced by increasing airbag pressure[10] however, since our system has no method to quantify air pressure, the inflation is controlled based on the subjective tolerability of the volunteer. The motion could be accounted for using rigid shifts of the PRS or the beam aperture analogous to current standard practice in image guided radiation therapy. An additional benefit of MR-guidance over CBCT for gantry-free systems is that no rotation of the imaging system with respect to the patient is required. Rigid shifts induced by rotation of the subject during CBCT imaging have been shown to cause blurring and require correction methods[21].

No correlation was present between 3D displacement magnitude and volunteer BMI however it was observed that the magnitudes of the displacement for the only male volunteer (volunteer 6) were noticeably smaller compared with the female volunteers. This variation may be due to the anatomical differences of the male pelvis compared with the female – however more male volunteers would be required to validate this hypothesis. A correlation was observed between volunteer BMI and average non-rigid deformation. This result is intuitive as a higher BMI likely indicates a higher volume of deformable adipose tissue around the pelvis but is limited however by the small number of volunteers and variation in BMI's (standard deviation 2.8).

Mean differences of -2.0 mm and -2.3 mm were observed between the measured and expected values for LR and SI shifts of the CIRS pelvic phantom, respectively. These shifts occurred in the same direction and were of comparable magnitude for each position, which were attributed to variations in the laser position relative to the cross-hair markings on the phantom and small lateral shifts of the flat-top couch on the MRI scanner, which occurred during phantom positioning.

Residual non-rigid tissue deformation were dominated by variations in external contours caused by rotation which presents a challenge for EBRT as the depth dose will be subsequently affected[16]. Additionally, non-rigid shifts cannot be readily accounted for with a rigid shift of the patient or the beam aperture. The impact of non-rigid deformation could be mitigated by optimising a treatment plan for each couch angle, however external deformation will likely change day to day – so a daily re-optimisation may be necessary with associated time and computation costs. An alternative approach could be strategic beam and couch angle placements to avoid regions of high external contour deformation, however deformation magnitude for each angle would need to be assessed on a daily basis to adapt to daily changes in deformations, and beam weightings updated to favour angles with lower deformation magnitudes. Internal motion was less pronounced and of the same magnitude as intra-fraction motion observed during a course of treatment. For instance, reported mean inter-fraction motion of the cervix can vary between 1.0 - 16.0 mm AP, 1.5 - 8.0 mm SI and 0.3 - 10.0 mm LR[31-33] with individual AP motion up to 63 mm[34]. Cree *et al.* note the use of adaptive radiation therapy is often targeted to patients with substantial motion during planning. It logically follows that the same approach with MRI-guidance may be applied to patients with intra-fraction motion introduced by rotation[35] with MRI-guided EBRT for cervical cancer having already been demonstrated on a Co^{60} system[36], however the rotation induced motions will further contribute to motion uncertainties which would need to be considered during treatment.

One limitation of this study was the inability of the non-rigid registration to fully match the internal anatomy, in particular when the external contour deformation was large (*Table 3*). This is due to a combination of reduced image quality in the fast acquisition (55 s) images, reduced image contrast in the central anatomy, and the high variability in soft tissue anatomy i.e. bladder filling and movement of the internal organs such as uterus and bowels[27] which cause variations in the shape and volume of organs being registered. The inability of the image registration to account for significant volume changes will have caused an underestimation of the mean deformation values. The maximum deformation results are unlikely to be affected since the registration performed well on the external contour where image contrast was high (*Table 3*). Future work will be required to adequately address the internal registration challenges, possibly incorporating a surface coil to improve the image quality, as it could result in variations in planned vs delivered dose. Given the high dose gradients that exist between tumour volumes and organs at risk, image registration uncertainties may have deleterious consequences during treatment if not corrected. Improved image quality would nonetheless need to be weighed up with a likely increase in required scan time, since maintaining short scan times would be desirable for an MRI-guided treatment scenario given the added time which will be required for patient set-up, position verification/adaption and treatment delivery. The internal registration accuracy may also be improved by including contour-based alignment prior to global registration at the expense of added time for contouring structures. Whelan *et al.* investigated prostate, rectum, and bladder contour motion during rotation on this system and found variations were within inter-contour variability following a prostate-guided rigid registration[17].

Image quality is a significant issue for radiation therapy due to the high geometric precision required[37] and is further complicated by patient rotation for several reasons. Firstly, the introduction of the PRS and the patient may create inhomogeneity and subsequent distortions in the main B_0 field. Perhaps more significantly, during the rotation the patient's position within the magnet shifts off-centre. While the B_0 and gradient uniformity within the centre of the magnet is well controlled, this is not the case further from the magnet centre at the edge of the patient. Rotation may also cause differences in B1 transmission with subsequent signal variation across an image which may compromise the quality of image registrations.

In this study we have shown that both distortion (Figure 12) and signal non uniformity (Figure 13) were minimal with no deleterious or additive effects observed. However, this should be evaluated for any MRI utilising patient rotation. The extent of image distortion as a function of distance from the isocentre has been previously investigated for the MRI scanner used in this study with distortions approaching 5 mm at radial distances of 450 mm and 175 mm SI from the imaging iso centre[38]. These magnitudes are consistent with the measurements taken with the oil filled phantom in this study and, though no geometric distortion was visible in the images, would need to be considered for planning due to the tight geometric restrictions in radiotherapy. Due to the binary thresholding process, any internal deformation within the oil volume were not detected. However, Walker *et al.* demonstrated deformation magnitudes on this system were most significant at the greatest distance from isocentre, as measured relative to a ground truth CT image[38].

Another limitation of the study relates to the volunteer cohort itself. The geometric restrictions of the MRI, and consequently the PRS, greatly restricts the size of volunteers that were eligible to participate. These restrictions resulted in a large representation of females given they are generally smaller than males. A more representative cohort would include a better comparison of male and female rigid and non-rigid motion and quantification of deformation for volunteers with larger BMI scores. To utilise MRI, this may only be possible with an open magnet system to facilitate the necessary space for a larger PRS. Additionally, the deformation results presented here were acquired in a single imaging session. It is anticipated that anatomical deformation will vary day-to-day, which are as yet unquantified.

A future aim of this work will be to assess and quantify to what extent the described deformation impact treatment planning, particularly given the observed variability across the volunteers. Optimal treatment angles and beams could then be devised for treatments incorporating patient rotation. In instances where deformation is minimal, i.e. patients with a BMI < 20, creating a treatment plan on the 0° image may be sufficient, while in patients with significant deformation, multiple plans generated on the angled images would be necessary. If angle specific plans were used, questions relating to dose summation and optimisation would need to be addressed.

Conclusion

Rigid and non-rigid deformation due to horizontal patient rotation have been quantified for a cohort of healthy volunteers. Left-right translations were the most significant rigid motion and were caused by lateral shifts within the airbag supports. This motion could be accounted for with rigid adjustments to the couch and/or beam aperture prior to treatment. Significant non-rigid deformation of the external surface were observed for some volunteers which were correlated with BMI, and if unaccounted for would likely compromise treatment. Future work is required to assess the dosimetric impact of these deformation in order to develop methods to facilitate the delivery of radiotherapy with patient rotation under MRI guidance.

Acknowledgements

The authors wish to thank Mr Phil Chlap from the Ingham Institute for Applied Medical Research for programming assistance during this work and the South West Sydney Cancer Therapy Centre Radiation Oncology Clinical Trials department for coordinating the recruitment of volunteers. JB acknowledges funding support from the Ingham Institute for Applied Medical Research and South West Sydney Cancer Therapy Centre. The project is supported by an NHMRC program grant (APP1132471). The time of the volunteers in this study is gratefully appreciated.

The authors have confirmed that any identifiable participants in this study have given their consent for publication.

References

1. Feain I, Court L, Palta J, Beddar S, Keall P. Innovations in radiotherapy technology. *Clinical Oncology.* 2017;29(2):120-128.
2. Atun R, Jaffray DA, Barton MB, et al. Expanding global access to radiotherapy. *The Lancet Oncology.* 2015;16(10):1153-1186.
3. Weinrich U. Gantry design for proton and carbon hadrontherapy facilities. Paper presented at: Proceedings of EPAC2006.
4. Whelan B, Gierman S, Holloway L, Schmerge J, Keall P, Fahrig R. A novel electron accelerator for MRI-Linac radiotherapy. *Med Phys.* 2016;43(3):1285-1294.
5. Raaymakers B, Jürgenliemk-Schulz I, Bol G, et al. First patients treated with a 1.5 T MRI-Linac: clinical proof of concept of a high-precision, high-field MRI guided radiotherapy treatment. *Physics in Medicine & Biology.* 2017;62(23):L41.
6. Liney GP, Whelan B, Oborn B, Barton M, Keall P. MRI-Linear Accelerator Radiotherapy Systems. *Clinical Oncology.* 2018;30(11):686-691.
7. Feain I, Coleman L, Wallis H, Sokolov R, O'Brien R, Keall P. Technical Note: The design and function of a horizontal patient rotation system for the purposes of fixed-beam cancer radiotherapy. *Med Phys.* 2017;44(6):2490-2502.
8. Liu P, Nguyen D, Feain I, O'Brien R, Keall P, Booth J. Real-time image-guided adaptive radiotherapy of a rigid target for a prototype fixed beam radiotherapy system. *Medical physics.* 2018.
9. Eslick EM, Keall PJ. The Nano-X Linear Accelerator: A Compact and Economical Cancer Radiotherapy System Incorporating Patient Rotation. *Technol Cancer Res Treat.* 2015;14(5):565-572.
10. Liu PZY, O'Brien R, Heng SM, et al. Development and commissioning of a full-size prototype fixed-beam radiotherapy system with horizontal patient rotation. *Medical physics.* 2018.
11. Whelan B, Welgampola M, McGarvie L, et al. Patient reported outcomes of slow, single arc rotation: Do we need rotating gantries? *Journal of medical imaging and radiation oncology.* 2017.
12. Katz RC, Wilson L, Frazer N. Anxiety and its determinants in patients undergoing magnetic resonance imaging. *Journal of behavior therapy and experimental psychiatry.* 1994;25(2):131-134.
13. McIsaac HK, Thordarson DS, Shafran R, Rachman S, Poole G. Claustrophobia and the magnetic resonance imaging procedure. *Journal of Behavioral Medicine.* 1998;21(3):255-268.
14. Brahme A. Optimization of stationary and moving beam radiation therapy techniques. *Radiotherapy and Oncology.* 1988;12(2):129-140.
15. Admiraal MA, Schuring D, Hurkmans CW. Dose calculations accounting for breathing motion in stereotactic lung radiotherapy based on 4D-CT and the internal target volume. *Radiotherapy and Oncology.* 2008;86(1):55-60.
16. Kairn T. Patient rotation during linac-based photon electron radiotherapy. *Journal of medical imaging and radiation oncology.* 2018;62(4):548-552.
17. Whelan B, Liney GP, Dowling JA, et al. An MRI-compatible patient rotation system—design, construction, and first organ deformation results. *Medical physics.* 2017;44(2):581-588.
18. McLaughlin P, Wygoda A, Sahijdak W, et al. The effect of patient position and treatment technique in conformal treatment of prostate cancer. *International Journal of Radiation Oncology* Biology* Physics.* 1999;45(2):407-413.
19. Olch AJ, Gerig L, Li H, Mihaylov I, Morgan A. Dosimetric effects caused by couch tops and immobilization devices: report of AAPM Task Group 176. *Medical physics.* 2014;41(6Part1).
20. Barber J, Shieh C-C, Counter W, et al. A CBCT study of the gravity-induced movement in rotating rabbits. *Physics in Medicine & Biology.* 2018;63(10):105012.

21. Shieh C-C, Barber J, Counter W, et al. Cone-beam CT reconstruction with gravity-induced motion. *Physics in Medicine & Biology.* 2018;63(20):205007.

22. Fedorov A, Beichel R, Kalpathy-Cramer J, et al. 3D Slicer as an image computing platform for the Quantitative Imaging Network. *Magn Reson Imaging.* 2012;30(9):1323-1341.

23. Tustison NJ, Avants BB, Cook PA, et al. N4ITK: improved N3 bias correction. *IEEE transactions on medical imaging.* 2010;29(6):1310.

24. Rivest-Hénault D, Dowson N, Greer PB, Fripp J, Dowling JA. Robust inverse-consistent affine CT–MR registration in MRI-assisted and MRI-alone prostate radiation therapy. *Medical image analysis.* 2015;23(1):56-69.

25. Modat M, Ridgway GR, Taylor ZA, et al. Fast free-form deformation using graphics processing units. *Computer methods and programs in biomedicine.* 2010;98(3):278-284.

26. Yushkevich PA, Piven J, Hazlett HC, et al. User-guided 3D active contour segmentation of anatomical structures: significantly improved efficiency and reliability. *Neuroimage.* 2006;31(3):1116-1128.

27. Brock KK, Mutic S, McNutt TR, Li H, Kessler ML. Use of image registration and fusion algorithms and techniques in radiotherapy: Report of the AAPM Radiation Therapy Committee Task Group No. 132. *Medical physics.* 2017;44(7):e43-e76.

28. Sharp G, Li R, Wolfgang J, et al. Plastimatch—An open source software suite for radiotherapy image processing. Paper presented at: Proceedings of the XVI'th International Conference on the use of Computers in Radiotherapy (ICCR), Amsterdam, Netherlands2010.

29. Liney G, Owen S, Beaumont A, Lazar V, Manton D, Beavis A. Commissioning of a new wide-bore MRI scanner for radiotherapy planning of head and neck cancer. *The British journal of radiology.* 2013;86(1027):20130150.

30. Chandra SS, Dowling JA, Engstrom C, et al. A lightweight rapid application development framework for biomedical image analysis. *Computer methods and programs in biomedicine.* 2018;164:193-205.

31. Han Y, Shin EH, Huh SJ, Lee JE, Park W. Interfractional dose variation during intensity-modulated radiation therapy for cervical cancer assessed by weekly CT evaluation. *International Journal of Radiation Oncology* Biology* Physics.* 2006;65(2):617-623.

32. Langerak T, Mens JW, Quint S, et al. Cervix motion in 50 cervical cancer patients assessed by daily cone beam computed tomographic imaging of a new type of marker. *International Journal of Radiation Oncology* Biology* Physics.* 2015;93(3):532-539.

33. Taylor A, Powell M. Conformal and intensity-modulated radiotherapy for cervical cancer. *Clinical oncology.* 2008;20(6):417-425.

34. Collen C, Engels B, Duchateau M, et al. Volumetric imaging by megavoltage computed tomography for assessment of internal organ motion during radiotherapy for cervical cancer. *International Journal of Radiation Oncology* Biology* Physics.* 2010;77(5):1590-1595.

35. Cree A, Livsey J, Barraclough L, et al. The Potential Value of MRI in External-Beam Radiotherapy for Cervical Cancer. *Clinical Oncology.* 2018;30(11):737-750.

36. Asher D, Padgett KR, Llorente RE, et al. Magnetic Resonance-guided External Beam Radiation and Brachytherapy for a Patient with Intact Cervical Cancer. *Cureus.* 2018;10(5).

37. Liney GP, Moerland MA. Magnetic resonance imaging acquisition techniques for radiotherapy planning. Paper presented at: Seminars in radiation oncology2014.

38. Walker A, Liney G, Holloway L, Dowling J, Rivest-Henault D, Metcalfe P. Continuous table acquisition MRI for radiotherapy treatment planning: Distortion assessment with a new extended 3D volumetric phantom. *Medical Physics.* 2015;42(4):1982-1991.